Broadband wide-angle multifunctional polarization converter via liquid-metal-based metasurface

Wu, Pin Chieh; Zhu, Weiming; Shen, Zhong Xiang; Chong, Peter Han Joo; Ser, Wee; Tsai, Din Ping; Liu, Ai-Qun

2017

Wu, P. C., Zhu, W., Shen, Z. X., Chong, P. H. J., Ser, W., Tsai, D. P., & Liu, A.-Q. (2017). Broadband wide-angle multifunctional polarization converter via liquid-metal-based metasurface. Advanced Optical Materials, 5(7), 1600938-. doi:10.1002/adom.201600938

https://hdl.handle.net/10356/139050

https://doi.org/10.1002/adom.201600938

WILEY-VCH

DOI: 10.1002/ ((please add manuscript number))
Article type: Full Paper

Broadband Wide-angle Multi-functional Polarization Converter via Liquid-metal based Metasurface

Pin Chieh Wu, Weiming Zhu, Zhong Xiang Shen, Peter Han Joo Chong, Wee Ser, Din Ping Tsai and Ai-Qun Liu**

P. C. Wu, W. M. Zhu, Z. X. Shen, H. J. Chong, W. Ser and A. Q. Liu*
School of Electrical and Electronic Engineering, Nanyang Technological University
Singapore 639798
E-mail: eaqliu@ntu.edu.sg

D. P. Tsai*
Research Center for Applied Sciences, Academia Sinica, Taipei 11529, Taiwan
Department of Physics, National Taiwan University, Taipei 10617, Taiwan
E-mail: dptsai@sinica.edu.tw

Keywords: (microfluidic metasurface, multi-functional polarization conversion)

Abstract

Metasurfaces enable flat optical components with predesigned functionalities, including the polarization conversion, using sub-wavelength elements. However, switching between different functionalities of the metasurface-based optical components is extremely difficult because sub-wavelength elements have to be finely addressed to change the spatial phase gradient for desired functionality. Here, we demonstrate, for the first time, a broadband wide-angle multi-functional polarization converter via galinstan-based metasurface with each element array actively addressed. The switching between different functionalities are realized by controlling L-shaped galinstan resonator using microfluidic channels, which maintain the optical performances, i.e. broadband and large angular tolerance, of the polarization converter. Furthermore, the galinstan-based metasurface is also demonstrated to function as a broadband optical attenuator, which provides prospects for various applications, such as smart radar, stealth technology and light manipulation for quantum communication.

1. Introduction

Polarization conversion is to transfer an electromagnetic (EM) wave with undefined or mixed polarization state into a predefined one, e.g. from linear-to-circular polarization. Multi-functional polarization conversion refers to the ability of adaptively transferring a fixed polarization state into any desired polarization state, including linear, circular and elliptical polarization states, which is not only useful in smart radar[1] but also in light manipulation for quantum communication[2-4]. Metasurface offers a promising approach for the control of polarization state because it enables abrupt local changes to the electromagnetic amplitude and phase of scattering light within a subwavelength spatial region[5-14]. Imposing orthogonal resonant modes within a metasurface element is crucial for the control of amplitude as well as the phase difference between two orthogonal spatial directions in order to achieve the polarization conversion[15-17]. In addition, it is possible to compensate the intrinsic dispersion by integrating a dielectric spacer and a metallic mirror with an array of metasurface to realize a broadband polarization conversion[18-20]. Large angular tolerance can also be achieved by using out-plane isotropic metasurfaces for impendence match under different incident angles[21, 22]. However, multi-functional polarization conversion is difficult to be realized using metasurface modulated by either changing the effective permittivity in surrounding environment or distance between building elements for entire pattern array[23-26]. The elements of those metasurfaces cannot be continuously controlled, which is difficult to change the function of the metasurface, e.g. from linear-to-circular to linear-to-elliptical polarization conversion, while maintaining the broadband and large angular tolerance of incidence. Some pioneer works show the possibility of controlling either single or metasurface array elements using microelectromechanical systems (MEMS)[27-30]. However, the complexity of the electric circuit addressing each element grows exponentially with the size of the array, which will inevitably affect the optical performance of the metasurface. Recently, liquid-based

metasurfaces[31] are demonstrated using water droplet[32] and liquid metal[33], which function as perfect absorber and tunable lens. However, multi-functional polarization converters are still lagging behind, especially those with broadband feature and large angular tolerance of incidence.

Here, we demonstrate, for the first time, a multi-functional polarization conversion with ultra-broad bandwidth and large angular tolerance. A microfluidic network addresses every galinstan-based metasurface element and controls their orthogonal resonant modes continuously. As proof of concept, a multi-functional polarization converter is demonstrated for linear-to-linear, linear-to-circular and linear-to-elliptical polarization conversions by controlling the galinstan within the microfluidic channels. The possibility of tuning the incident EM wave to any desired polarization state suggests intriguing new opportunity to create active devices with dynamic polarization control.

2. Results and Discussion

2.1. Design of Multi-Functional Polarization Converter

The element of the galinstan based metasurface is shown in **Figure 1**b, which consists of L-shaped resonators and microfluidic channels with one inlet and two outlets. The microfluidic channels are formed by bonding two polydimethylsiloxane (PDMS) layers, which are bonded to a perfect electric conductor (PEC) substrate. The L-shaped resonator has two arms, which are controlled continuously and actively by the pressure of the two outlets. **Figures 1**c and **1**d show the symmetric and asymmetric L-shaped resonators when the arm lengths L_x and L_y are equivalent and inequivalent, respectively. The galinstan based metasurface consist of three layers, as shown in **Figure 1**a. A PEC layer eliminates the transmitted light and enhances the reflection performance. A dielectric PDMS spacer (thicknesses H) provides a spatial region

for cavity-like resonance and a square lattice array of L-shaped resonators. The polarization state of the reflected light is dominated by the phase and amplitude of the two eigenmodes[7], which can be tuned by controlling the arm length of the L-shaped resonators. Therefore, the galinstan metasurface functions as a polarization converter with multiple functionalities, including linear-to-linear, linear-to-circular and linear-to-elliptical polarization conversions.

2.2. Numerical Analysis

The multi-functional polarization converter is numerically characterized by solving the Maxwell's equation using finite-integration technique (FIT) under periodic boundary conditions. The L-shaped resonator exhibits two orthogonal resonant eigenmodes[34] (symmetric and asymmetric modes) when the incident electric field is along or perpendicular to the symmetric axes of the structure as shown in **Figure 2**. The slight difference between simulated and measured co-polarization reflection is due to the fabrication errors such as the variations of microfluidic channel dimensions and PDMS thickness between the numerical design and the fabricated sample. These two orthogonal resonant eigenmodes dominate the polarization state of the reflected light. For example, an x-polarized reflected light can be generated when both the amplitude and phase of the two eigenmodes are identical. Other polarization states, including circular and elliptical polarization, can be generated by tuning the phase and amplitude of those two eigenmodes, which are excited simultaneously by an *x*- or *y*-polarized incident light[18]. **Figure 3** shows the reflection spectra of co-polarized and cross-polarized light at different arm length, L_x and L_y, when the incident light is linear polarized along the *y*-direction. The right column shows the *z*-component of the electric field (E_z) distribution when the incident frequency f is 12 GHz. Linear cross-polarization conversion can be achieved when $L_x = L_y = 5$ mm as shown in **Figure 3**a. On the other hand, the incident light is converted into a circularly polarized one when the cross-polarized and co-

polarized reflection have identical amplitude and π/2 phase difference as shown in **Figure 3**b (see **Figure 6**a for detailed information). The intensity of the cross-polarized reflection drops as the symmetry of the L-shaped resonators is broken by tuning the arm length as shown in **Figure 3**c. This can be further verified by examining the *z*-component of the electric field distribution. The asymmetric near-field patterns on various L-shaped resonators show that both symmetric and asymmetric eigenmodes are excited[35]. The strength ratio and phase difference between the two eigenmodes are changed when L_x and L_y are varying, which changes the polarization state of the reflected light. The proposed L-shaped resonators are expected to have a large angular tolerance of incidence due to the out-plane isotropic structural configuration of L-shaped resonators when the phase retardation induced by tilted incidence is trivial. In addition, the near-field coupling between excited eigenmodes and their imaging charges results in an effective magnetic response, which strongly depends on the thickness of dielectric spacer *H*. The multi-functional polarization converter becomes broadband with optimized *H*, which is shown in **Figure S1**.

2.3. Experimental Results and Discussions

The multi-functional polarization converter consists of 30 × 30 L-shaped resonators with a period of 6 mm as shown in **Figure 4**a. The thickness *H* of PDMS layer between the PEC substrate and the L-shaped resonators is 2 mm, which is optimized for broadband operation of the multi-functional polarization converter. The L-shaped resonator has two orthogonal arms, which can be continuously and actively tuned from 0.6 mm to 5 mm by substituting hydrochloric acid (HCl) vapor with galinstan within the microfluidic channels. The pressures between the input and output of the microfluidic channel are controlled by syringe pumps and regulated by the pneumatic valves[33, 36, 37]. To eliminate the influence upon the optical responses from the injection channels, the liquid-metal is expelled out from liquid-metal input

channels before S-parameter measurement. **Figures 4**b to **4**c show the zoom-in view of L-shaped resonators with different L_x and L_y. Here, galinstan is implemented because of its high conductivity, nontoxic property and superior to mercury for applications that require a liquid-metal at room temperature[38]. The high conductivity also assists the L-shaped resonators in providing the resonance features of broadband polarization conversion with high efficiency (Supplementary **Figure S2**).

The experimental characterizations of the multi-functional polarization converter are performed in a microwave anechoic chamber using a vector network analyzer with two horn antennas as the wave source and the receiver. The incident EM wave is linearly polarized with the electric field parallel to the surface of the polarization converter. The incident angle is tuned from 2˚ to 60˚. The polarization conversion is demonstrated by tuning the arm length L_x and L_y while maintaining the symmetry of the L-shaped resonators $L_x = L_y$. Here, the linear-to-linear cross polarization conversion ratio (PCR) is defined as

$$PCR = \frac{R_{xy}}{R_{yy} + R_{xy}} \tag{1}$$

where R_{ij} indicates the reflection coefficient of the i component generated by a j-polarized EM wave (i, j = x, y). The spectral profile of the PCR under different incident angles is shown in **Figure 5** when the arm length is fixed at $L_x = L_y$ = 3.8 mm. The working bandwidth can reach 86 % of the central frequency according to the numerical analysis as shown in **Figure S3**. The measured working bandwidth is 61.6% of the central frequency, which is limited by the measurement range of the receiving horn antenna (up to 18 GHz). When the incident angle is increased with transverse electric (TE) mode, the incident electric field maintains at the same direction related to the L-shaped resonators, which will not deteriorate the electric response of the L-shaped resonators. Thus a broadband polarization conversion with large angular tolerance of incidence is realized. **Figures 5**b and **5**c show the numerical and experimental results, respectively, for the contour map of

PCR as the function of incident frequency and angle, which agree with each other well. The difference between simulation and measurement results mainly arises from the fabrication errors, and the alignment issue during the S-parameter measurement for different angles of incidence. The multi-functional polarization converter maintains a broad working bandwidth when the incident angle is less than 45°. Further increasing the incident angle results in the shrink of working bandwidth. Therefore, the multi-functional polarization converter is demonstrated to have broad working bandwidth with large angular tolerance of incidence.

The switching between the functionalities, e.g. from linear-to-linear polarization conversion to linear-to-circular polarization conversion, is experimentally characterized by fixing the incident EM wave at randomly chosen frequency f = 12 GHz as shown in **Figure** 6a. The *x*-component and *y*-component of the reflected EM wave are measured separately when the incident EM wave is *y*-polarized. The reflection coefficient and phase difference between *x*-component and *y*-component are defined as $\Delta R = R_{xy} - R_{yy}$ and $\Delta\phi = \phi_{xy} - \phi_{yy}$, respectively, where φ_{ij} presents the reflected phase of the i component generated by a j-polarized illumination ($i, j = x, y$). The reflected EM wave has no *x*-component (ΔR = -1) when the arm length $L_x = L_y$ within the range of 1.5 mm to 2.2 mm. The polarization converter functions as a perfect reflector. ΔR increases from -1 to 0 and $\Delta\phi$ remains $\pi/2$ when the arm length is increasing. The polarization converter functions as a linear-to-elliptical polarization converter. The linear-to-circular polarization conversion is realized when $L_x = L_y$ = 3 mm. A linear cross polarization conversion is subsequently achieved when the arm length is within the range from 3.3 mm to 4.8 mm. Furthermore, the broad working bandwidth can be realized for linear-to-elliptical and linear-to-circular by tuning the arm length. The numerical analysis shows that the linear-to-circular polarization conversion can

be realized in a broad working bandwidth, which is 107.7% of the central frequency (Supplementary **Figure S4**).

Beside switchable polarization conversion, a broadband tunable optical attenuation function is also demonstrated by breaking the symmetry of the L-shaped resonators as shown in **Figure 6**b. A modulation depth[25] factor here is introduced to evaluate the performance on tunable attenuation function. It is defined as the absolute value of maximum achievable intensity change relative to the reference case of the minimum reflection intensity at each frequency, that is, $\text{modulation depth} = \left| \frac{R_{\text{cross,min.}}(f) - R_{\text{cross,max.}}(f)}{R_{\text{cross,max.}}(f)} \right|$, where the first subscript represents the cross-polarization state of reflection is carried out for evaluation. As the arm length L_x is swept from 0.6 mm to 3.8 mm while L_y is fixed at 3.8 mm, a wide range of reflection intensity in linear cross polarization can be reached actively within a broad frequency window. It can conclude that such proposed microfluidic metasurface exhibits an ultra-high attenuation function operating in whole interested spectral range because of the smoothly changed reflection intensity in linear cross-polarized state.

3. Conclusion

In conclusion, we demonstrated, for the first time, a broadband multi-functional polarization converter with large angular tolerance of incidence using galinstan-based metasurface. The reflected EM wave can be converted to three different polarization states, including linear, circular and elliptic polarization states, by tuning the arm length of the L-shaped resonators. In the experiment, it measures a broad working bandwidth larger than 60% of central frequency and a large angular tolerance of 45°. Furthermore, the broadband reflection and optical attenuation functionalities are also demonstrated. The multi-functional polarization

converter provides prospects for various applications, such as smart radar, stealth technology and light manipulation for quantum technology.

4. Experimental Section

The S-parameters are measured in an anechoic chamber using a vector network analyzer (Agilent N5230A) and two dual polarization horn antennas (WJ-48430), as shown in Supplementary **Figure S5**. The distance between two horn antennas (as source and receiver) and microfluidic metasurface is maintained at 1.2 m. The polarization state of source antenna is fixed along *y*-axis while the amplitude and phase signals are measured by *x*-polarized or *y*-polarized receiver antennas for cross-polarized and co-polarized reflection, respectively. The incident angle dependence measurements are carried out by rotating the source and receiver antennas. All the measurement results are normalized to the reflection spectra of the copper plate with the same incident angle.

Supporting Information

Supporting Information is available from the Wiley Online Library or from the author.

Acknowledgements

The work is mainly supported by Singapore Ministry of Education (MOE) (Grant No. RG89/13), Singapore National Research Foundation under its Competitive Research Program (Award number: NRF-CRP13-2014-01 & Project number: NRF2014NRF-CRP001-002), Ministry of Science and Technology, Taiwan (Grant No. MOST-105-2745-M-002-002-ASP) and Academia Sinica (Grant No. AS-103-TP-A06). The authors are also grateful to National Center for Theoretical Sciences, NEMS Research Center of National Taiwan University, National Center for High-Performance Computing, Taiwan, and Research Center for Applied Sciences, Academia Sinica, Taiwan for their supports.

Received: ((will be filled in by the editorial staff))
Revised: ((will be filled in by the editorial staff))
Published online: ((will be filled in by the editorial staff))

References

[1] C. Barry, *Smart Mater. Struct.* **1999**, 8, 64.
[2] L. Sansoni, F. Sciarrino, G. Vallone, P. Mataloni, A. Crespi, R. Ramponi, R. Osellame, *Phys. Rev. Lett.* **2010**, 105, 200503.
[3] R. Heilmann, M. Gräfe, S. Nolte, A. Szameit, *Sci. Rep.* **2014**, 4, 4118.
[4] R. M. Stevenson, R. J. Young, P. Atkinson, K. Cooper, D. A. Ritchie, A. J. Shields, *Nature* **2006**, 439, 179-182.
[5] Y.-W. Huang, W. T. Chen, W.-Y. Tsai, P. C. Wu, C.-M. Wang, G. Sun, D. P. Tsai, *Nano Lett.* **2015**, 15, 3122-3127.
[6] N. Yu, F. Capasso, *Nat. Mater.* **2014**, 13, 139-150.
[7] N. Yu, F. Aieta, P. Genevet, M. A. Kats, Z. Gaburro, F. Capasso, *Nano Lett.* **2012**, 12, 6328-6333.
[8] M. Khorasaninejad, F. Aieta, P. Kanhaiya, M. A. Kats, P. Genevet, D. Rousso, F. Capasso, *Nano Lett.* **2015**, 15, 5358-5362.
[9] X. Chen, L. Huang, H. Mühlenbernd, G. Li, B. Bai, Q. Tan, G. Jin, C.-W. Qiu, S. Zhang, T. Zentgraf, *Nat. Commun.* **2012**, 3, 1198.
[10] B. Walther, C. Helgert, C. Rockstuhl, F. Setzpfandt, F. Eilenberger, E.-B. Kley, F. Lederer, A. Tünnermann, T. Pertsch, *Adv. Mater.* **2012**, 24, 6300-6304.
[11] F. Aieta, P. Genevet, N. Yu, M. A. Kats, Z. Gaburro, F. Capasso, *Nano Lett.* **2012**, 12, 1702-1706.
[12] X. Zhang, Z. Tian, W. Yue, J. Gu, S. Zhang, J. Han, W. Zhang, *Adv. Mater.* **2013**, 25, 4567-4572.
[13] X. Yin, Z. Ye, J. Rho, Y. Wang, X. Zhang, *Science* **2013**, 339, 1405-1407.
[14] N. Meinzer, W. L. Barnes, I. R. Hooper, *Nat. Photon.* **2014**, 8, 889-898.
[15] H. F. Ma, G. Z. Wang, G. S. Kong, T. J. Cui, *Opt. Mater. Express* **2014**, 4, 1717-1724.
[16] L.-J. Black, Y. Wang, C. H. de Groot, A. Arbouet, O. L. Muskens, *ACS Nano* **2014**, 8, 6390-6399.
[17] J. Hao, Q. Ren, Z. An, X. Huang, Z. Chen, M. Qiu, L. Zhou, *Phys. Rev. A* **2009**, 80, 023807.
[18] S.-C. Jiang, X. Xiong, Y.-S. Hu, Y.-H. Hu, G.-B. Ma, R.-W. Peng, C. Sun, M. Wang, *Phys. Rev. X* **2014**, 4, 021026.
[19] L. Cong, N. Xu, J. Gu, R. Singh, J. Han, W. Zhang, *Laser Photon. Rev.* **2014**, 8, 626-632.
[20] N. K. Grady, J. E. Heyes, D. R. Chowdhury, Y. Zeng, M. T. Reiten, A. K. Azad, A. J. Taylor, D. A. R. Dalvit, H.-T. Chen, *Science* **2013**, 340, 1304-1307.
[21] Z. H. Jiang, L. Lin, D. Ma, S. Yun, D. H. Werner, Z. Liu, T. S. Mayer, *Sci. Rep.* **2014**, 4.
[22] C.-C. Chen, A. Ishikawa, Y.-H. Tang, M.-H. Shiao, D. P. Tsai, T. Tanaka, *Adv. Opt. Mater.* **2015**, 3, 44-48.
[23] B. Gholipour, J. Zhang, K. F. MacDonald, D. W. Hewak, N. I. Zheludev, *Adv. Mater.* **2013**, 25, 3050-3054.
[24] W. M. Zhu, A. Q. Liu, T. Bourouina, D. P. Tsai, J. H. Teng, X. H. Zhang, G. Q. Lo, D. L. Kwong, N. I. Zheludev, *Nat. Commun.* **2012**, 3, 1274.
[25] Y. Yao, R. Shankar, M. A. Kats, Y. Song, J. Kong, M. Loncar, F. Capasso, *Nano Lett.* **2014**, 14, 6526-6532.
[26] M. Lapine, I. V. Shadrivov, D. A. Powell, Y. S. Kivshar, *Nat. Mater.* **2012**, 11, 30-33.
[27] Y. H. Fu, A. Q. Liu, W. M. Zhu, X. M. Zhang, D. P. Tsai, J. B. Zhang, T. Mei, J. F. Tao, H. C. Guo, X. H. Zhang, J. H. Teng, N. I. Zheludev, G. Q. Lo, D. L. Kwong, *Adv. Funct. Mater.* **2011**, 21, 3589-3594.

[28] W. M. Zhu, A. Q. Liu, X. M. Zhang, D. P. Tsai, T. Bourouina, J. H. Teng, X. H. Zhang, H. C. Guo, H. Tanoto, T. Mei, G. Q. Lo, D. L. Kwong, *Adv. Mater.* **2011**, 23, 1792-1796.
[29] T. Hand, S. Cummer, *IEEE Antennas Wireless Propag. Lett.* **2007**, 6, 401-404.
[30] J. Perruisseau-Carrier, T. Lisec, A. K. Skrivervik, *Microw Opt. Technol. Let.* **2006**, 48, 2496-2499.
[31] J. Wang, S. Liu, A. Nahata, *Opt. Express* **2012**, 20, 12119-12126.
[32] Y. J. Yoo, S. Ju, S. Y. Park, Y. Ju Kim, J. Bong, T. Lim, K. W. Kim, J. Y. Rhee, Y. Lee, *Sci. Rep.* **2015**, 5, 14018.
[33] W. Zhu, Q. Song, L. Yan, W. Zhang, P.-C. Wu, L. K. Chin, H. Cai, D. P. Tsai, Z. X. Shen, T. W. Deng, S. K. Ting, Y. Gu, G. Q. Lo, D. L. Kwong, Z. C. Yang, R. Huang, A.-Q. Liu, N. Zheludev, *Adv. Mater.* **2015**, 27, 4739-4743.
[34] M. A. Kats, P. Genevet, G. Aoust, N. Yu, R. Blanchard, F. Aieta, Z. Gaburro, F. Capasso, *Proc. Natl. Acad. Sci.* **2012**, 109, 12364-12368.
[35] B. J. Bohn, M. Schnell, M. A. Kats, F. Aieta, R. Hillenbrand, F. Capasso, *Nano Lett* **2015**, 15, 3851-3858.
[36] T. Thorsen, S. J. Maerkl, S. R. Quake, *Science* **2002**, 298, 580-584.
[37] M. A. Unger, H.-P. Chou, T. Thorsen, A. Scherer, S. R. Quake, *Science* **2000**, 288, 113-116.
[38] M. D. Dickey, R. C. Chiechi, R. J. Larsen, E. A. Weiss, D. A. Weitz, G. M. Whitesides, *Adv. Funct. Mater.* **2008**, 18, 1097-1104.

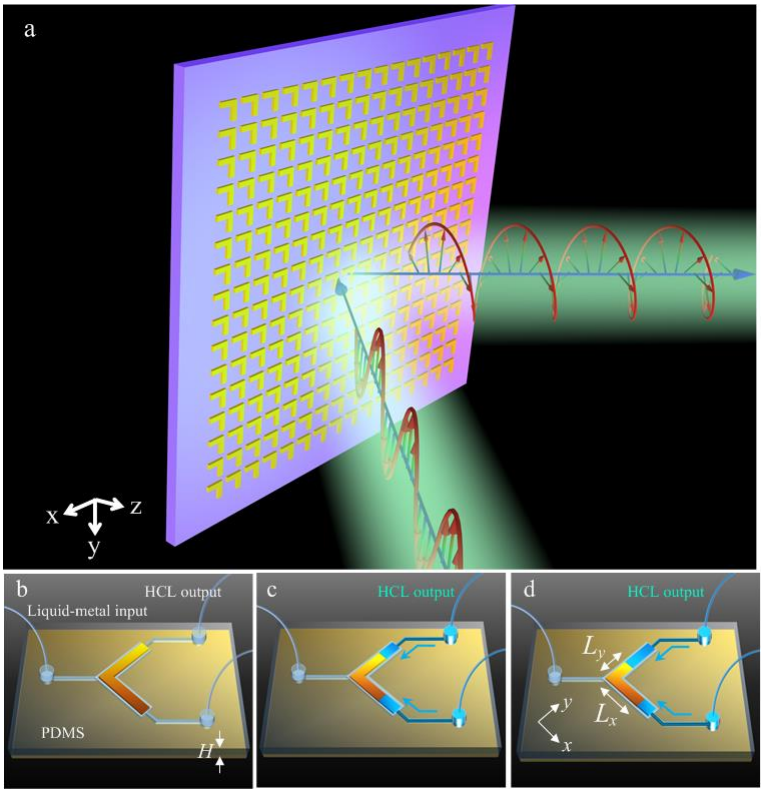

Figure 1. Schematic of multi-functional polarization converter. a) The overview of the polarization converter based on an elaborately engineered metasurface. The liquid-metal L-shaped resonators are used as the building blocks. b) A symmetric L-shaped resonator with fixed 5-mm arm length and 0.6-mm width with balanced pressure between the two HCL output. Individual injection of HCL expells away the liquid-metal and forms symmetric c) and asymmetric d) tuning of the arm length. *H*: thickness of PDMS spacer layer.

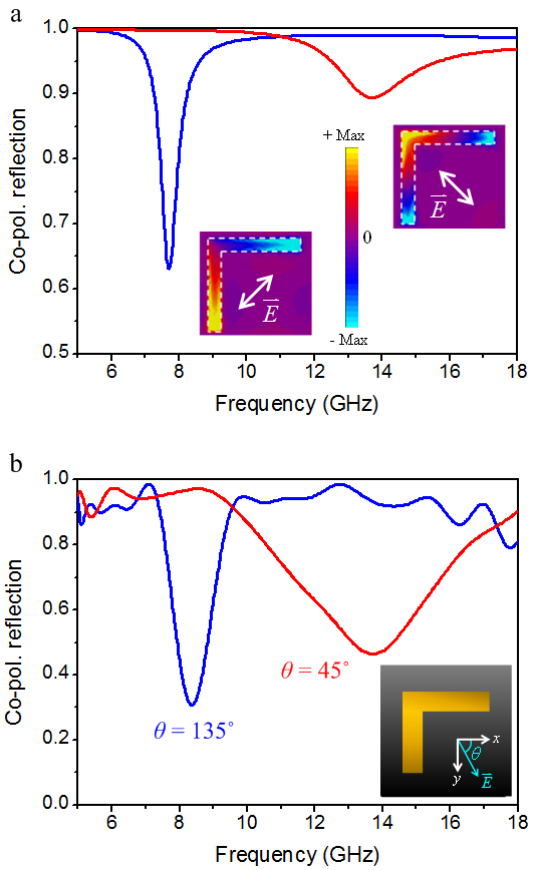

Figure 2. The Orthogonal eigenmodes of L-shaped resonators. a) Simulated and b) experimental spectra for a symmetric L-shaped resonator array with L_x = L_y = 5 mm under normal illumination. The incident electric field is along 45˚ (red curve) and 135˚ (blue curve) for the excitation of two orthogonal resonant modes. The top inset shows *z*-component of the electric field. The bottom inset shows schematic for the direction of incident electric field related to the *x*-axis. The polarization states of the reflected EM wave are dominated by the phase and amplitude of those two eigenmodes, which are excited simultaneously by an *x*- or *y*-polarized incidence.

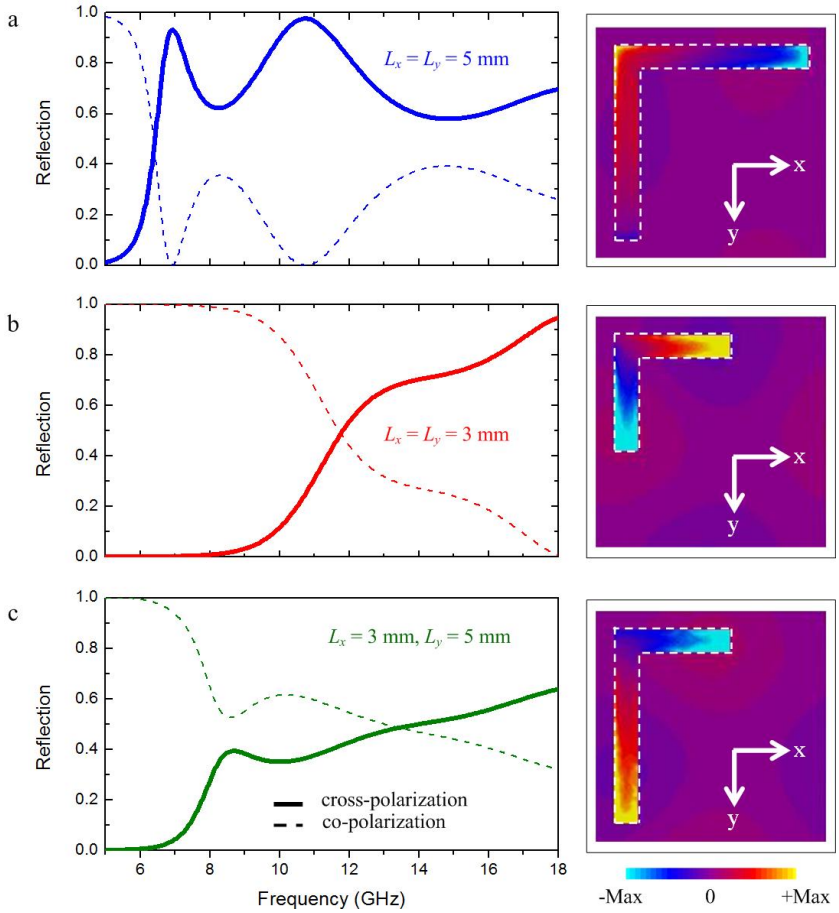

Figure 3. Reflection spectra and *z*-component of the electric field for different L-shaped resonators. Left column shows the reflection spectra for galinstan-based metasurface with different arm lengths a) $L_x = L_y = 5$ mm, b) $L_x = L_y = 3$ mm and c) $L_x = 3$ mm, $L_y = 5$ mm. All the incident fields are along the *y*-direction. Right column shows the amplitude of near-field electric field (*z*-component) at frequency $f = 12$ GHz. The PDMS spacer thickness is 2 mm. The asymmetric near-field patterns show that both symmetric and asymmetric eigenmodes are excited and controlled by the arm lengths, which dominate the polarization state of the reflected EM wave.

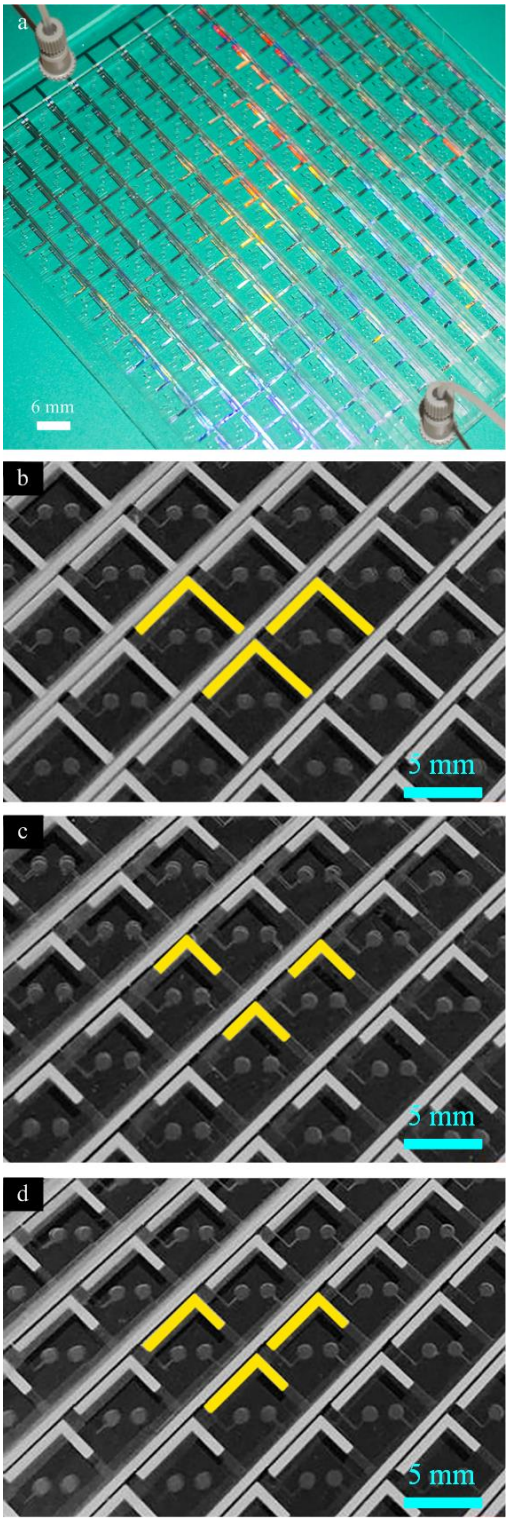

Figure 4. Photographs of the multi-functional polarization converter. a) An overview photograph of dynamic microfluidic metasurface. b) Zoomed-in view of the microfluidic metasurface after galinstan completely filling-in. c,d) The arm length of L-shaped resonators is managed when HCl vapor pushes galinstan away from the cavity forming symmetric c) and asymmetric d) resonators.

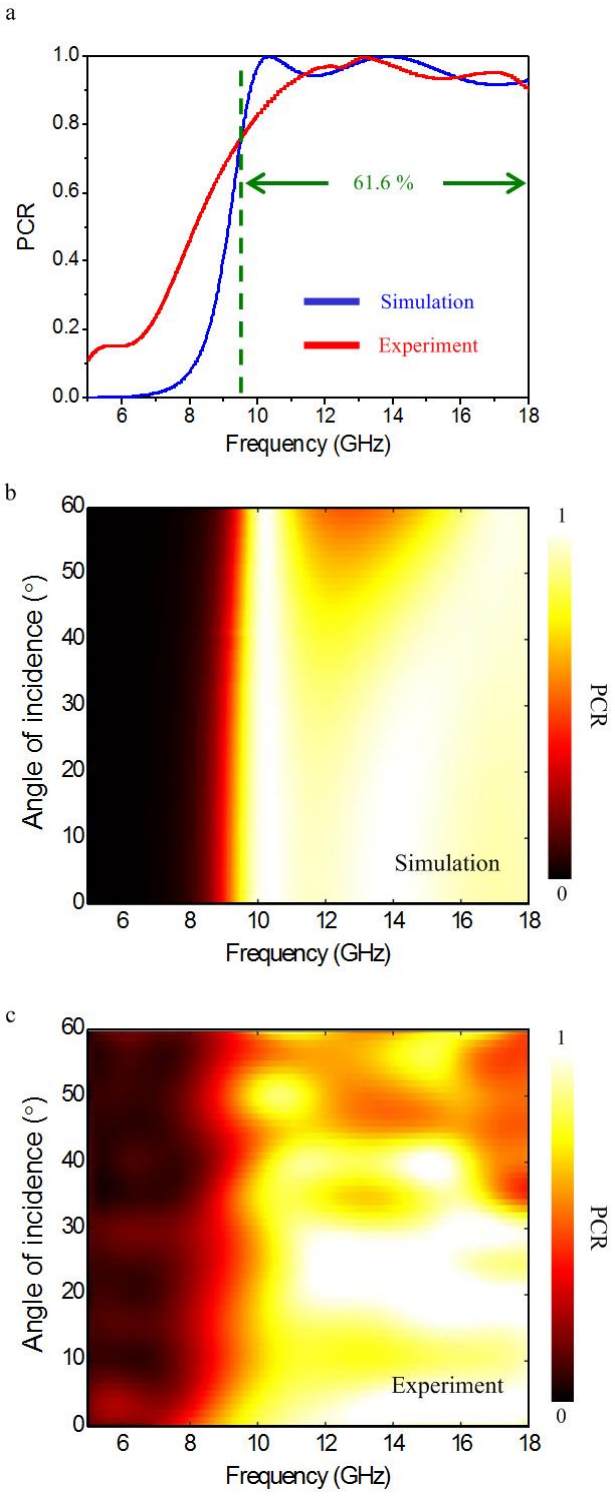

Figure 5. Linear-to-linear cross polarization conversion. a) Simulated (blue line) and measured (red line) linear polarization conversion ratio (PCR) as a function of frequency under normal illumination. b) Simulated and c) measured PCR at a various angle of incidences. The thickness of PDMS dielectric spacer is fixed as 2 mm.

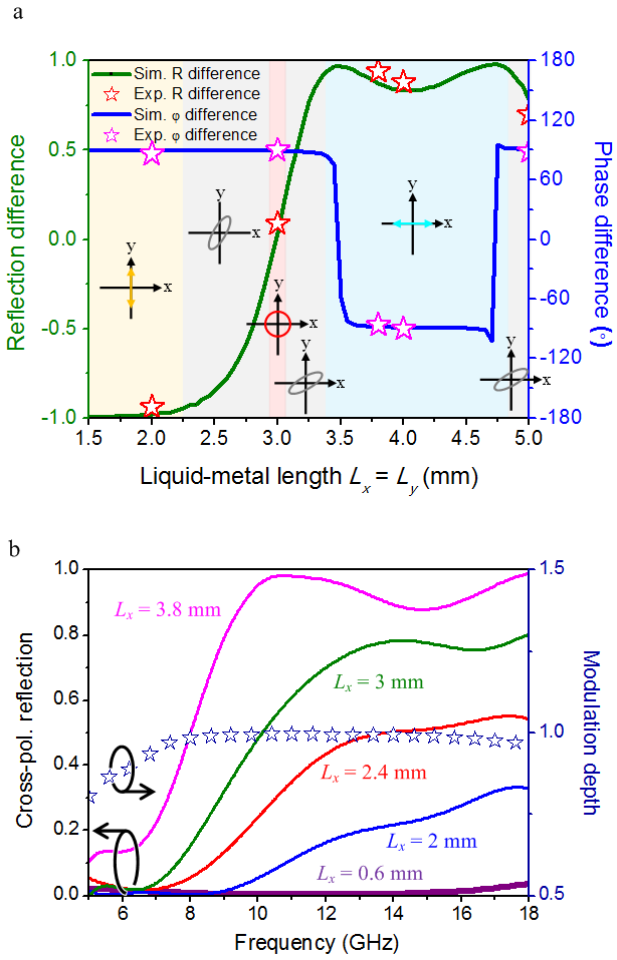

Figure 6. Multi-functional polarization conversion and tunable optical attenuation. a) Reflection and phase differences as a function of liquid-metal length in symmetric L-shaped antennas. Curves and starts indicate the simulated and experimental results, respectively. Here, the incident frequency f = 12 GHz. b) Experimental results of tunable optical attenuation for cross-polarized reflection using asymmetric liquid-metal L-shaped resonators when L_y is fixed at 3.8 mm. The incident EM wave is *y*-polarized with incident angle of 2˚.